An exploration of the ballistic resistance of multilayer graphene polymer composites

M.R. O'Masta*, B.P. Russell and V.S. Deshpande

Engineering Department, University of Cambridge, Trumpington Street, Cambridge CB2 1PZ, UK

Abstract

The response of multilayer graphene / polyvinyl alcohol (MLG/PVA) films were studied under edge-clamped quasi-static (Q.S.) and dynamic transverse loading. The 10 μm thick films, reinforced by ~35 vol.% MLG and measuring 85 mm square were fabricated by liquid exfoliation of the graphene followed by filtration of the MLG/PVA dispersion. The responses of the MLG/PVA films were compared with those of equal areal mass films of pure PVA and aluminum. The moderately conductive (~10^{-2} S cm^{-1}) MLG/PVA films had a Young's modulus approximately twice that of PVA and a low strain rate (10^{-3} s^{-1}) peak strength that was about 50% higher. Moreover, while the MLG/PVA films had a tensile strength lower than the Al films, they were stiffer and had a higher load carrying capacity compared to the Al films and were stiffer than the PVA films under Q.S. transverse loading. The ballistic limit of the MLG/PVA films was ~50% higher than the Al films but the higher ductility of the parent PVA resulted in the pure PVA films having a higher ballistic resistance. The ballistic resistance of the MLG/PVA is well predicted by a membrane stretching analysis and this enables us to present an outlook on the ballistic resistance potential of graphene/PVA composites comprising aligned large flakes.

Keywords: Polymer composites; Graphene; Failure; Impact

* Corresponding author: M.R. O'Masta; E-mail address: mro27@cam.ac.uk

1. Introduction

Graphene is part of a larger class of 2D materials, which includes among others BN, MoS_2, $NbSe_2$ and TaS_2 [1]. These 2D materials and graphene in particular have received considerable recent attention due to their many exceptional properties, including 2.3% absorption in the white light spectrum, high surface area, very high thermal and electrical conductivity, impermeability to gas and exceptional mechanical stiffness and strength [2]. Potential applications of graphene range from flexible electronics and photonic devices to barrier films and paints to sensors and bio-applications [2]. Advanced multifunctional composites is an additional area that also is ripe to benefit from graphene's electrical and mechanical properties. This study assesses the response of high volume fraction graphene-polymer composites in under edge-clamped quasi-static and dynamic loading, with an aim to reveal the potential of such composites for ballistic resistance applications.

The fabrication of composite systems requires large quantities of graphene at low production cost. This can be achieved using a top-down approach, based on the exfoliation of graphene from graphite, rather than the bottom-up approaches (e.g. chemical vapor deposition and epitaxial growth) that produce higher quality flakes [3]. Developed methods for mechanical exfoliation are sonication, ball milling, fluid dynamics and supercritical fluid [3]. Paton et al. [4] have shown the liquid exfoliation of graphene using high-shear forces can create large graphene quantities of consistent quality (~10 nm thick multi-layer graphene platelets of in-plane dimensions ~0.4 μm). Furthermore, with the liquid exfoliation method, polymers can be introduced to stabilize the exfoliated graphene as part of the fabrication method.

Graphene has been used as a reinforcement in a range of thermosets and thermoplastics [5–7]. Very small volume fractions are needed to surpass the percolation limit and conductivity

values above 0.01 S cm^{-1} are achievable from at most a few volume percent of graphene [5,6]. Furthermore, graphene reinforcement can increase the parent material's glass transition temperature, and cause large increases in the tensile strength and Young's modulus, albeit with significant decreases in ductility [6–8]. For instance, many studies using polyvinyl alcohol (PVA) as a filler (attractive for its solubility in water and ability to stabilize graphene during liquid exfoliation) have reported increases up to 100% in strength and modulus as well as moderate conductivity levels with the addition of a few volume percentage of graphene [9–14]. However, most studies have been limited to small strains and quasi-static loading.

The impact response of 10-100 nm thick sheets of pure multi-layer graphene (MLG) when impacted by a ~4 μm diameter silicon sphere was studied by Lee et al. [15]. The material behaved as a thin membrane and failed by a tensile "petalling" mode: such petalling failure modes are commonly observed in thin metal plates [16,17] and fiber reinforced composite laminates with a low matrix shear strength [18–20]. Phoenix and Porwal [21] analytically solved the limiting impact velocity (commonly referred to as the ballistic limit V_{bl}), of such membrane type structures subject to normal impact. This predicted ballistic limit scales primarily with the tensile strength of the membrane. With graphene having an intrinsic strength of 130 GPa [22] and a near isotropic in-plane response, a composite reinforced with graphene has the potential to surpass the composites of high performance fibers (e.g. aramids, UHMPWE, PBO and PIPD).

This study examines this potential by investigating the quasi-static and dynamic transverse loading response of a 10 μm thick multilayer graphene / polyvinyl alcohol (MLG/PVA) composite film with ~35 vol.% MLG. We first report the tensile response, toughness and electrical conductivity of the composite. These measured material properties are used to interpret the measured transverse loading responses of the MLG/PVA films under static as well as

dynamic loading (ballistic loading), and these measurements contrasted with the performances of equal areal mass films of pure PVA and 99% purity aluminum. Comparisons with an analytical membrane-stretching model are presented and this model then extended to present an outlook on the ultimate ballistic potential of graphene composites comprising large well-aligned flakes in PVA.

2. Film materials and fabrication

2.1. Sample materials

All films had an areal density of $a \approx 0.017$ kg m^{-2} (see Table 1). The multilayer graphene / polyvinyl alcohol (MLG/PVA) composite film was fabricated from graphite powder (CAS: 7782-42-5; Fisher Scientific UK, Loughborough, UK) and PVA (MW: ~27,000; CAS: 9002-89-5; Sigma Aldrich Company Ltd., Dorset, UK) using the procedure described subsequently. Fabrication of the pure PVA film followed the same procedure, with the exception of the graphite addition. The aluminum foil was purchased from Goodfellow Cambridge Ltd. (Huntingdon, UK).

2.2. MLG/PVA fabrication

Dispersion production: We liquid-exfoliated polymer-stabilized graphene following the procedure introduced in Paton et al. [4]. First, 25 g of graphite powder was added to a 250 mL solution of 0.4 wt.% PVA in distilled water. Next, to exfoliate the graphite, the solution was mixed by a model L5M high-shear laboratory mixer (Silverson Machines Ltd., Chesham, UK) equipped with a 25.4 mm outer diameter, square hole high shear screen and operated at 7000 RPM for 90 min. The dispersion was then centrifuged for 30 min. at 1950 RCF to encourage settling of the unexfoliated graphite. Finally, the supernatant was collected for filtration.

Table 1: The areal density a_x, density ρ_x and effective thickness t_x of the three material systems investigated here. The subscript 'x' for denotes 'c', 'p' or 'al' for the composite, PVA and Al films, respectively. The densities of Al and PVA are quoted from Ref. [23].

Material	a_x (g m^{-2})	ρ_x (kg m^{-3})	t_x (μm)
MLG/PVA	16.5±0.5	1590±30	10.3
PVA	17.4±0.1	1190	14.6
Al	17.0±0.0	2700	6.3

Filtering equipment: Recovery of a composite film from the dispersion was carried out using the pressure filtration system sketched in Fig. 1. An aluminum grate with a hexagonal pattern of 1 mm diameter holes with a 1.3 mm center-to-center spacing was placed at the bottom of the vessel. Two filter papers were placed on top of this grate: (i) a 2-3 μm pore size qualitative filter paper (grade 55, Fisher Scientific, Loughborough UK) in contact with the grate and (ii) a 0.2 μm pore size, Whatman Nuclepore membrane (purchased from Sigma Aldrich Company Ltd.) on top of this filter paper. The dispersion was then poured onto these filter papers as shown in Fig. 1. The Nuclepore membrane resisted passage of the PVA and graphene platelets while the qualitative filter paper and aluminum grate provided flexural support. Rubber stoppers placed between the vessel body and the filter papers, around the borders, prevented fluid leakage.
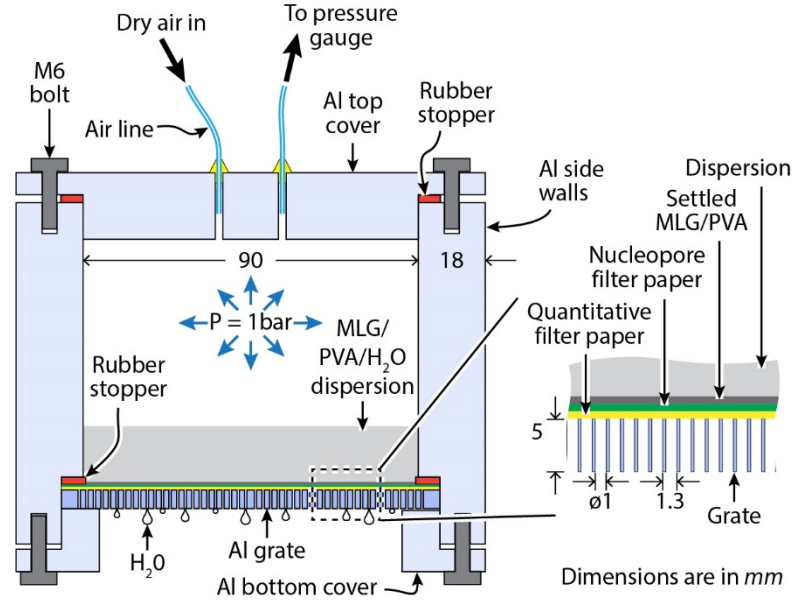
Figure 1: Sketch of the filtration equipment and procedure for the fabrication of the MLG/PVA composite films.

Filtering procedure: 250 mL of the dispersion was poured into the pressure vessel. The internal pressure was raised to 1 bar and held until the liquid filtered from the vessel (~12 hr.). The Nuclepore membrane, with the hydrated MLG/PVA film coating, was removed from the vessel and placed under a lid to dry for 24hr. The dried MLG/PVA film was then separated from Nuclepore membrane and stored in a dehumidifier.

Physical properties: An image of the resulting MLG/PVA film is shown in Fig. 2a. The dispersion side of the film is dimpled from the filtering procedure as seen in the magnified view in Fig. 2b. A through-thickness cross-section of a sample torn due to impact loading is shown in Fig. 2c. There is distinct layering associated with the alignment of the MLG platelets in the plane of the film.
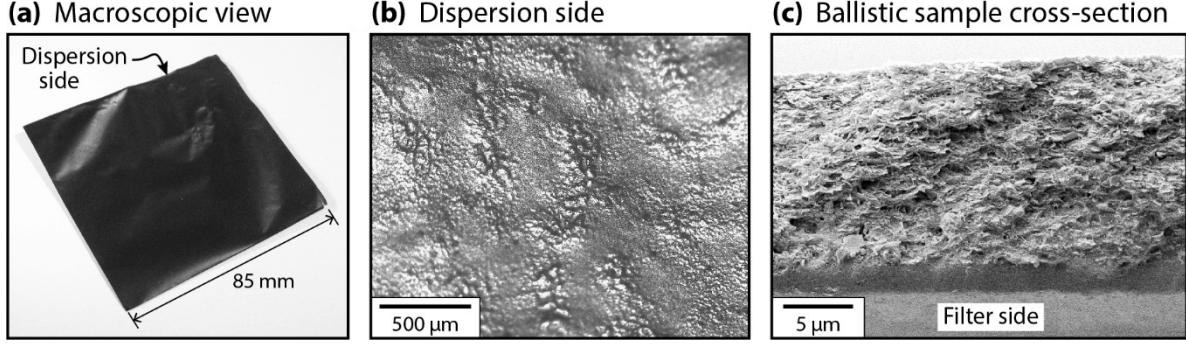
Figure 2: (a) Oblique photograph of a MLG/PVA film. (b) Optical image of the dispersion side of the film. (c) Through-thickness, cross-sectional SEM micrograph of a film torn by the impact of a $m_p = 20$ mg projectile traveling at $V_0 = 16.3$ m s^{-1}.

The presence of multilayer graphene (MLG) platelets within the film was confirmed using wide-angle X-ray diffraction. The full-width half mass of the (002) peak revealed each graphite platelet comprised ~30 graphene layers on average (measurement details are provided as supplementary information, S1). This is consistent with the AFM measurements from Ref. [4], whose liquid-exfoliation method for the graphene was replicated here.

The measured mass per unit area or areal density a_c of the film is listed in Table 1. Also shown is the measured density ρ_c of a 100 mg sample of the MLG/PVA film using helium pycnometry (performed by Quantachrome UK Ltd., Hartley Wintney, UK). These two measurements allow the calculation of the mean film thickness $t_c \equiv a_c/\rho_c$ as listed Table 1. Moreover, assuming a negligible void volume within the films, the volume fraction ϕ_g of the graphene within the films can be obtained from the rule of mixtures as

$$\phi_g = \frac{\rho_c - \rho_p}{\rho_g - \rho_p},\qquad(1)$$

where $\rho_c = 1590 \pm 30$ kg m^{-3}, $\rho_g = 2260$ kg m^{-3} and $\rho_p = 1190$ kg m^{-3} are the densities of the composite, graphene and PVA, respectively, as listed in Table 1. This gives an upper bound

estimation of the graphite volume fraction as $\phi_g = 0.37 \pm 0.03$ (where the uncertainty is associated pycnometry measurement error of ρ_c).

3. Mechanical and electrical properties

3.1. Tensile behavior

Methodology: Rectangular samples 1.3 mm wide were cut by razor blade. Paper tabs were glued to either end to give a 20 mm gauge length between the tabs. The tabs were gripped using rubber lined friction grips attached to a model 5544 Instron (High Wycombe, UK), equipped with a 5 N load cell. Each sample was pulled at a constant rate of displacement corresponding to a nominal strain rate of either $\dot{\varepsilon} = 10^{-3}$ s^{-1} or 10^{-1} s^{-1}. Five repeat tests were conducted in each case to gauge the scatter in the measurements.

Table 2: The Young's modulus E_x, peak tensile strength σ_x, tear resistance T_x and electrical conductivity Σ_x of the three materials investigated here. The subscript 'x' denotes 'c', 'p' or 'al' for the composite, PVA and Al films, respectively. The conductivity measurements for PVA and Al are taken from Ref. [23].

| Material | Tension | | | | Tear | Conductivity |
| | $\dot{\varepsilon} = 10^{-3}$ s^{-1} | | $\dot{\varepsilon} = 10^{-1}$ s^{-1} | | | |
	E_x (GPa)	σ_x (MPa)	E_x (GPa)	σ_x (MPa)	T_x (kJ m^{-2})	Σ_x (S cm^{-1})
MLG/PVA	6±0.6	55±5	8±0.7	90±3	2.9±0.1	$2\times10^{-2}\pm1\times10^{-2}$
PVA	2.5±0.3	35±4	5±0.4	120±5	11.5±0.6	1×10^{-12}
Al	35±1	182±5	35±1	185±3	3.7±0.1	3×10^{5}

Results: The nominal stress versus strain responses of the MLG/PVA film are shown in Fig. 3a for two representative tests at each applied strain rate $\dot{\varepsilon}$. At $\dot{\varepsilon} = 10^{-3}$ s^{-1}, the material is approximately linear elastic up to a peak stress at $\varepsilon\sim1.5\%$. This is followed by a softening response with catastrophic failure at $\varepsilon\sim4\%$. The modulus and peak strength values are tabulated

in Table 2. At the high strain rate of $\dot{\varepsilon} = 10^{-1}\,\mathrm{s}^{-1}$, the modulus and peak stress increase by 30% and 60%, respectively (see Table 2) and the material response switches to elastic-brittle as seen in Fig. 3a.

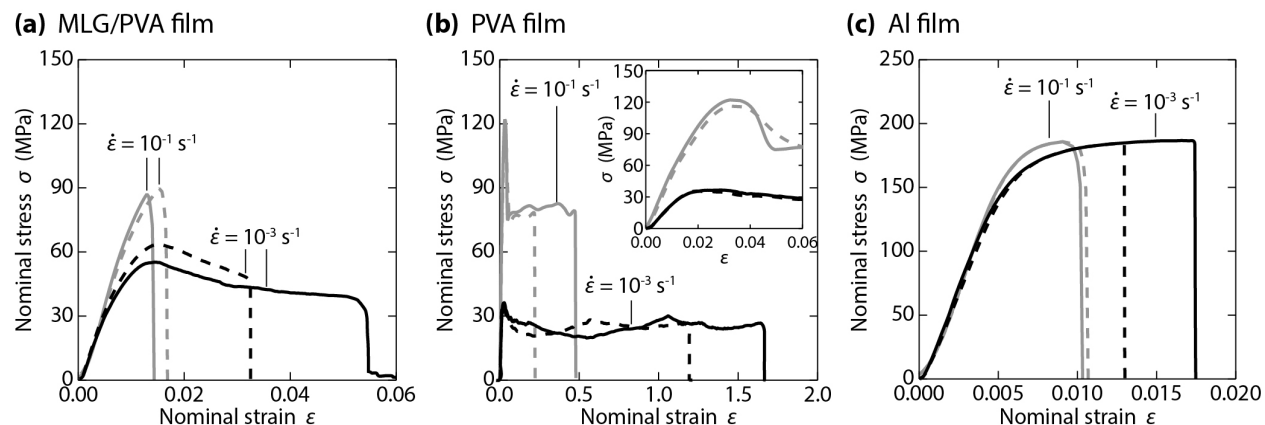**(a)** MLG/PVA film   **(b)** PVA film   **(c)** Al film

Figure 3: The uniaxial nominal tensile stress versus strain responses of the (a) MLG/PVA (b) PVA and (c) Al films. Two representative curves are shown for each applied strain rate $\dot{\varepsilon}$. In (b) an inset showing the early strain response is included.

The modulus and peak strength of the PVA film strained at $\dot{\varepsilon} = 10^{-3}\,\mathrm{s}^{-1}$ were substantially lower than the values measured for the MLG/PVA composite films (Fig. 3b). However, the PVA film was more ductile with a ductility >100%. Further, the PVA films had a significantly higher strain rate sensitivity with its peak strength increasing by nearly a factor of four as the strain rate was increased from $\dot{\varepsilon} = 10^{-3}\,\mathrm{s}^{-1}$ to $10^{-1}\,\mathrm{s}^{-1}$. In fact at these high strain rates the PVA film had a 33% higher peak strength compared to the MLG/PVA film (see Table 2). Conversely, the Al foil showed little if any strain rate sensitivity (Fig. 3c) but had a considerably higher modulus and peak strength compared to the MLG/PVA film and a very low ductility.

The ultimate graphene composite: "Ultimate" graphene/polymer composites are composites comprising defect-free, single layer graphene flakes of sizes in excess of the shear

lag length (calculated to be on the order of 10 μm [28, 29]) that are perfectly aligned with the loading direction. Such composites will have an in-plane modulus E_c and strength σ_c given by the rule of mixtures as

$$E_c = \phi_g E_g + \left(1 - \phi_g\right)E_p \quad \& \quad \sigma_c = \phi_g \sigma_g + \left(1 - \phi_g\right)\sigma_p \ , \qquad (2)$$

where E and σ are respectively the modulus and strength, and subscripts g and p denotes the property as belonging to either the graphene flakes or polymer matrix, respectively. The basic material parameters are well established, i.e. $\sigma_g = 100$ GPa and $E_g = 1000$ GPa for defect-free graphene flakes [22] and $\sigma_p = 100$ MPa and $E_p = 5$ GPa for PVA. For the $\phi_g = 0.35$ composite considered here, the predicted modulus and strength of the ultimate composite is $E_c = 350$ GPa and $\sigma_c = 35$ GPa, respectively.

The properties of the graphene composites manufactured and tested are well below these upper bound predictions, with measured values of $E_c = 6$ GPa and $\sigma_c = 0.05$ GPa. The primary causes for this poor performance are thought to be related to: (i) the small in-plane platelet sizes (~0.4 μm [4]) and the large number (~30) of graphene layers comprising a platelet place mean that the platelets are much smaller than the sizes required by shear-lag theory for efficient load transfer into the graphene; and (ii) relatively poor alignment of the platelets in the plane of the films. Additional effects such as the presence of defects, such as voids, are also expected to play a role in reducing the strength and modulus.

3.2. Toughness

The tear resistance ("trouser tear" toughness) was measured following the procedure is ASTM D1938 [24] (details on sample geometry and test response are provided as supplementary information, S2). The tear toughness T_x for each material x reported in Table 2 is ratio of the measured plateau load and the half thickness of the film averaged over three repeat tests. The

PVA film was the toughest, consistent with the large ductility observed from the tensile measurements. The MLG/PVA and Al films had a similar toughness that was only ~25% of the PVA value.

3.3. Electrical conductivity

A four-terminal sensing set-up was used to measure the electrical conductivity Σ_c of the MLG/PVA film (the experimental details are given as supplementary information, S3). The film is moderately conductive with $\Sigma_c \sim 0.01 - 0.04$ S cm^{-1} (over five different samples). This conductivity value is similar to other graphene and graphene-oxide composites studied in the literature [5,6], and is in contrast to the insulating nature of PVA as seen in Table 2.

4. Transverse loading test protocol

The main aim of this study is to investigate the ballistic potential of MLG/PVA composites. However, given the observed strain rate sensitivity of the tensile response (Table 2), the transverse loading of the films was investigated under two conditions: (i) application of a constant rate of low displacement rate (CRD), and (ii) projectile impact (PI) at a given impact (initial) velocity. In both cases, a film measuring 40 mm × 40 mm was clamped between an aluminum plate containing a 30 mm diameter hole and a 0.5 mm thick steel ring with inner and outer diameters 30 and 60 mm, respectively on a pitch circle of diameter 45 mm (Fig. 4a). The clamping pressure was provided by twelve equally spaced circular magnets of diameter 8 mm embedded in flat bottom holes within the aluminum plate. The surface of the steel ring in contact with the film was lined with a 0.5 mm rubber sheet to increase the friction and evenly distribute the clamping pressure.
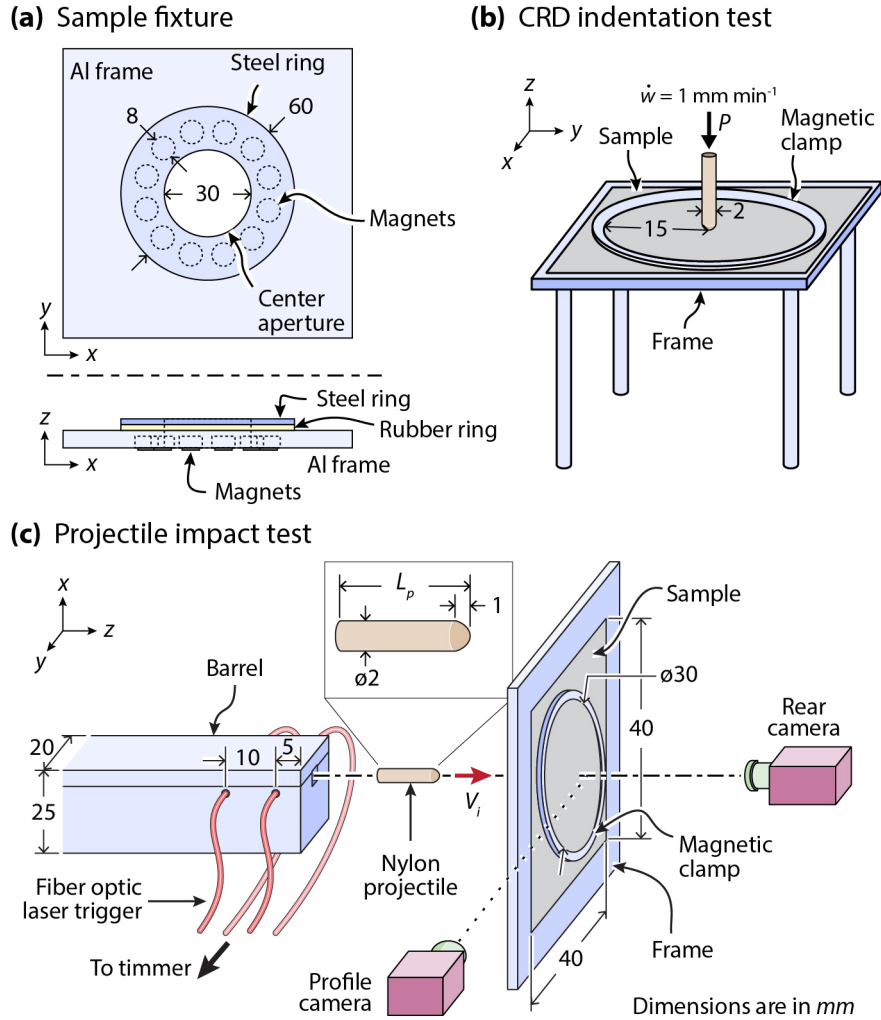
Figure 4: Sketches of the (a) clamping fixture for the films, (b) the constant rate of displacement (CRD) quasi-static loading test, and (c) a side view of the projectile impact (PI) experiment showing the test specimen and gas gun muzzle. All dimensions are in mm.

4.1. Constant rate of displacement (CRD) quasi-static test

The clamped films were loaded centrally and normally by a hemi-spherically tipped nylon rod of diameter $d_p = 2\,\text{mm}$. The indenter rod was attached to a 5544 model Instron and displaced at a rate $\dot{w} = 1\,\text{mm min}^{-1}$, and the applied load measured via the 5N load cell of the test machine. Loading was continued until the films perforated.

12

4.2. Projectile impact

Cylindrical nylon rods of diameter $d_p = 2$ mm and length L_p with a hemispherical tip were fired from the gas gun to impact the films centrally and normally (Fig. 4c) at a velocity V_0. Details of test procedure and gas gun setup are provided in as supplementary information, S4.

The length L_p sets the mass m_p of the projectile. The tests were conducted with $m_p = 6, 20$ and 36 mg (the 6 mg projectile was a 2 mm diameter sphere). Following Cunniff [25], we present results in terms of the non-dimensional areal mass ratios of the film and projectile, i.e. $\Gamma_0 = \rho_a \pi d_p^2 / (4m_p) = \{8.9, 2.7 \text{ and } 1.5\} \times 10^{-3}$. Tests were conducted with increasing V_0 (in steps of $\sim??\,\text{ms}^{-1}$) for a given Γ_0 until the films failed, with failure defined as the appearance of a through-thickness crack in the post-impact inspection of the specimen. The mean of the highest impact velocity where the film survived and the lowest impact velocity where the film failed is defined as the ballistic limit V_{bl}.

5. Quasi-static transverse loading

The measured applied load P versus indenter displacement w response of the MLG/PVA film is plotted in Fig. 5a (for clarity only a single representative measurement from the three tests is included). The displacement $w \gg$ film thickness implying that the response is dominated by the stretching of the film with negligible contribution from film bending. This results in an increasing slope dP/dw as the film deflects and aligns with the applied load. A peak load is attained at $P \approx 0.5$ N and the applied load then drops catastrophically to about 0.05 N. This is associated with the formation of petals, i.e. radial cracks (Fig. 5b.i) and these cracks then propagate at an almost constant applied load [25] until complete failure of the film at $w \approx 2$ mm.

(a) Response

(b) Optical images of failed specimens
- **(i)** MLG/PVA film — Crack, Petal, Glare
- **(ii)** PVA film — Wrinkle, Tear
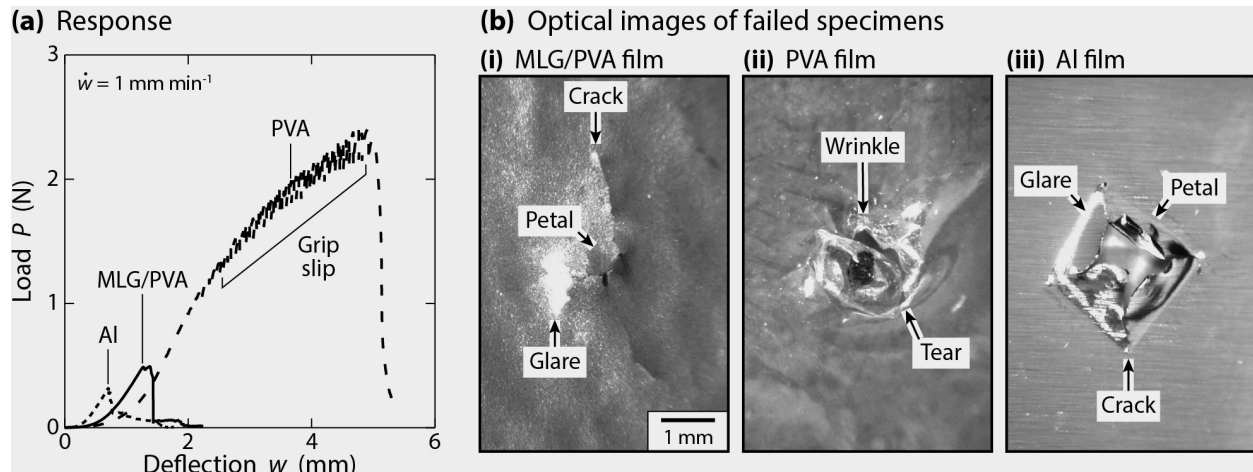- **(iii)** Al film — Glare, Petal, Crack

Figure 5: (a) Representative load-displacement responses of the three materials under CRD quasi-static transverse loading. (b) Post-mortem optical images of the rear surfaces of the three sample types. Artifacts as a result of glare are marked along with the observed cracks.

The lower PVA modulus implied that the PVA film was initially weaker under transverse loading but its higher ductility allowed the film to deflect more compared to the MLG/PVA film and better align with the load thereby reaching a higher peak load. Moreover, the failure of the film at peak load was by the formation of a circumferential crack (Fig. 5b.ii) allowing the indenter to push through the film immediately on the formation of this crack. We note that the large forces sustained by the PVA film resulted in slippage of the film at grips giving rise to a saw-tooth portion of the $P-w$ curve as marked in Fig. 5a. This slippage allowed further alignment of the film with the load as more material was dragged from within the grips towards the applied load. Thus, we anticipate the displacement at the failure of the film (and consequently the applied load) is higher in these experiments compared to the case if grip slippage was inhibited.

The Al film had a response similar to the MLG/PVA film though the higher modulus of Al implied that it was initially stiffer as seen in Fig. 5a. However, the Al film had a lower failure load which was due to: (i) the higher modulus of the Al implied the load and stresses within the

14

Al film increased more sharply with increasing w compared to the MLG/PVA films, and (ii) the lower ductility of the Al implies that the Al films can sustain smaller strains prior to failure. Therefore despite the Al having a much higher tensile failure stress, the Al films had a smaller load carrying capacity under quasi-static transverse loading compared to the MLG/PVA films.

6. Loading by projectile impact (PI)

6.1. Results

The measured ballistic limit velocities V_{bl} for the three films are plotted in Fig. 6a as a function of the projectile mass m_p. The vertical error bars indicate the two limiting velocities V_0 from which V_{bl} is calculated as the mean as described in Section 4.2. In all cases V_{bl} decreases with increasing m_p. Over the full range of m_p values investigated here, the MLG/PVA film outperforms the equal areal mass Al film with a V_{bl} almost twice that of the Al film. Moreover, the MLG/PVA film has a ballistic resistance only about 20% lower than the PVA film in spite of the PVA film having a significantly superior performance under quasi-static loading (Fig. 5a).

An optical image of the rear surface of the failed MLG/PVA film is shown in Fig. 6b.i. The images show that similar to the quasi-static case (Fig. 5b.i) the failure mode is again petalling. Moreover, an SEM micrograph (Fig. 6b.ii) shows an uneven failure surface indicative of tearing by pull-out the MLG platelets. By contrast, the failure mode of the PVA film changes from circumferential crack formation under quasi-static loading (Fig. 5b.ii) to failure by the formation of radial cracks and associated petalling (Fig. 6b.iii) under projectile impact. Further, SEM micro-graphs of the failure surface (Fig. 6b.iv) indicate brittle failure with the failure surface is flat showing so-called "river patterns". This embrittling of the PVA under high rate loading (also mirrored in the tensile tests, Fig. 3c) results in the failure mode changing to petalling and its ballistic limit being lower than anticipated and similar to the MLG/PVA films.
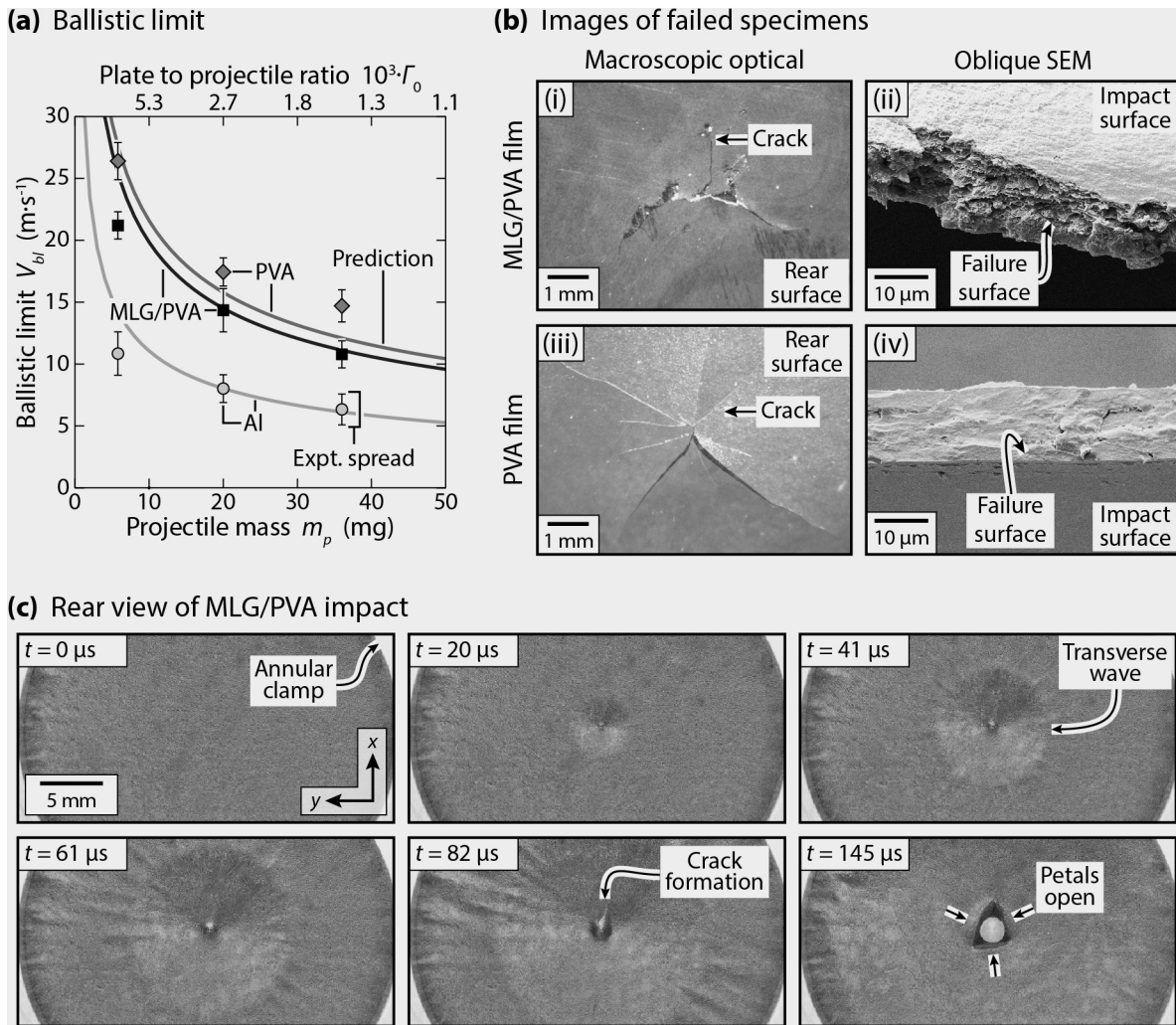
Figure 6: (a) The measured ballistic limit V_{bl} (symbols) as function of the projectile mass m_p (lower x-axis) or areal density ratio Γ_0 (upper x-axis). The vertical bars indicate the uncertainty in the measurement. Predictions using Eq. (3) are shown by the solid lines. (b) Images of post-impact failed MLG/PVA and PVA films (impact by a $m_p = 20$ mg projectile at $V_0 = 16.3$ and 18.6 m s^{-1} for the MLG/PVA and PVA films, respectively). (c) A montage of high-speed photographs showing the "dead-man" view of the MLG/PVA film impacted by the $m_p = 20$ mg projectile at $V_0 = 16.7$ m s^{-1}. Time $t = 0$ is the instant the projectile impacts the film.

A high-speed photographic sequence of the rear surface (so-called "dead-man view") of a MLG/PVA film impacted at $V_0 = 16.7$ m s^{-1} by the $m_p = 20$ mg projectile is shown in Fig. 6c

with time $t = 0$ defined as the instant the projectile impacts the film. A transverse elastic wave is seen to emanate from the impact site and travels towards the supports as analyzed by Phoenix and Porwal [21]. A crack is seen to initiate immediately under the projectile at $t \approx 82$ μs and the transverse wave impinges on the supports shortly after. The projectile is seen to come through the film by the formation of large petal cracks $t \approx 145$ μs. Very similar observations were made for the PVA and Al films and hence high-speed images of those impact events are not shown here for the sake of brevity.

6.2. Prediction of the ballistic resistance

The high-speed photography discussed in Section 6.1 reveals that the deformation and failure modes of the films is consistent with that assumed by Phoenix and Porwal [21] in their membrabe stretching analysis. Specifically, Phoenix and Porwal [21] presented an analytical model for the ballistic limit of elastic-brittle circular membranes impacted centrally and normally by rigid projectiles. Their analysis predicted that the ballistic limit scales with the Cunniff [25] velocity c^* via

$$\frac{V_{bl}}{c_x^*} = 2^{\frac{1}{3}} \varepsilon_x^{\frac{1}{12}} \frac{(1 + \Gamma_0)}{K_{max}^{3/4}} \,, \tag{3}$$

where $\varepsilon_x \equiv \sigma_x / E_x$ is the failure strain and the Cunniff velocity for material x is given by:

$$c_x^* = \frac{1}{2^{1/3}} \left(\frac{\sigma_x}{\rho_x}\right)^{2/3} \left(\frac{\rho_x}{E_x}\right)^{1/6} . \tag{4}$$

In Eq. (3), the strain magnification factor

$$K_{max} \approx \exp\left[-\frac{4\Gamma_0}{3(1 + \Gamma_0)}(\psi_{max}^2 - 1)\right] \psi_{max}^{1/3} \left[\frac{\sqrt{\psi_{max}/\varepsilon_p}(\psi_{max} - 1)}{\ln\left[1 + \sqrt{\psi_{max}/\varepsilon_p}(\psi_{max} - 1)\right]}\right], \tag{5}$$

with ψ_{max} the non-dimensional position

$$\psi_{max} \approx \sqrt{\frac{1 + \Gamma_0}{2\Gamma_0}} \ , \qquad\qquad (6)$$

of the transverse hinge at the instant of failure. Predictions of V_{bl} using Eq. (3) and the material parameter values for the three films as listed in Table 2 are included in Fig. 6a. Excellent agreement is observed confirming that the tensile membrane stretching failure mode assumed by Phoenix and Porwal [21] is the operative failure mode under projectile impact for all the three films types tested here.

6.3. Outlook of the ballistic resistance of ultimate graphene composites

The graphene composites manufactured and tested in this study have a performance well below the full potential due to the manufacturing issues discussed in Section 3.1. However, it is instructive to quantify the full potential of the ultimate graphene/PVA composites in anticipation of future manufacturing advances.

The strain dependence on the right-hand side of Eq. (3) is mild for practical values of failure strains ($\varepsilon \leq 0.04$). Thus, the ballistic limit can be expressed in the form $V_{bl}/c_x^* = f(\Gamma_0)$ as first hypothesized by Cunniff [25], i.e. the non-dimensional ballistic limit V_{bl}/c_x^* is only a function of the areal mass ratio Γ_0 and therefore the material metric c_x^* characterizes the ballistic resistance capacity of a material x when membrane stretching is the operative failure mechanism. The experiments reported here suggest that membrane stretching is expected to be the operative failure mode pf graphene composites and therefore we shall use this model to quantify the ballistic potential of ultimate graphene/PVA composites.

While the graphene composites manufactured and tested here have a relatively low tensile strength and modulus, Eq. (2) can be employed to predict the in-plane modulus E_c and strength σ_c of the ultimate graphene/PVA composites discussed in Section 3.1. Using Eq. (3), we plot in

18

Fig. 7a the Cunniff velocity c_c^* for ultimate graphene/PVA composites as a function of the graphene volume fraction ϕ_g (the PVA and graphene densities are given in Section 2.2 and mechanical properties in Section 3.1). The Cunniff velocity increases with increasing ϕ_g and is remarkably high even at relatively small volume fractions of graphene.
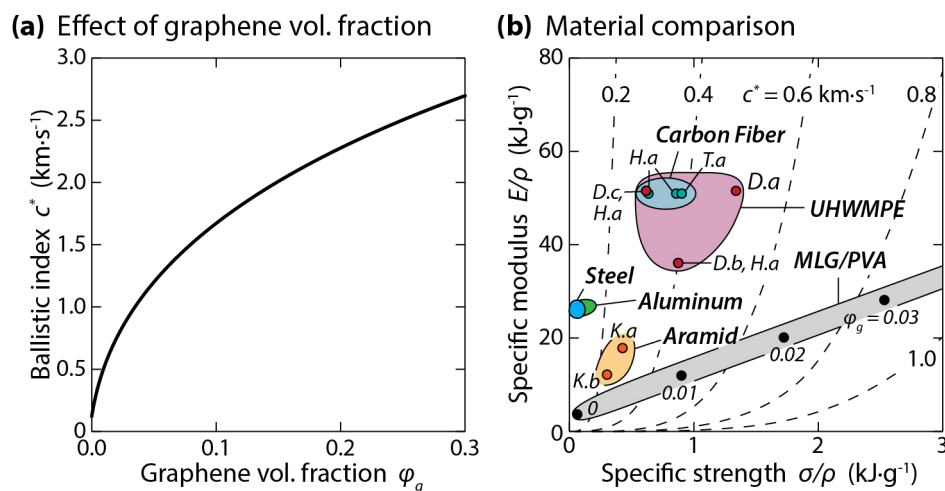

(a) Effect of graphene vol. fraction   **(b)** Material comparison

Figure 7: (a) Prediction of the Cunniff velocity c_c^* versus graphene volume fraction ϕ_g for ultimate graphene/PVA composites. (b) An Ashby chart with axes of specific strength and stiffness with contours of c^*. The chart shows the location of high performance commercial composites and ultimate graphene/PVA composites with $\phi_g \leq 3.5\%$. The abbreviations and references for used in (b) are listed in the footnote[1].

    In order to illustrate the remarkable performance of these ultimate graphene composites we include in Fig. 9b an Ashby-chart with axes of specific strength and specific modulus. Contours of the Cunniff velocity are marked on the chart along with the locations of key high-performance commercial composites currently as ballistic resistant materials. These include carbon, ultra-high molecular weight polyethylene (UHMWPE) and aramid fiber based composites as well as some

---

[1] Aluminum (2024, 60601, 7075 [23]); Aramid: K.a (Gold Shield GV2018; tested following procedure in [26]), K.b (Kevlar 29/PP [27]); Carbon fiber: H.a (Hexply 8552 [19,28]), T.a (Torray T800H [29]); Steel (AISI 1020, AISI 4130, AISI 4340 [23]); and UHMWPE: D.a (Dyneema HB212 [26]), D.b (HB50 [30]), D.c (Dyneema BT10 [30]), S.a (Spectra Shield II SR3136 [31]) H.a (Tensylon HSBD30A [26]).

widely used metals such as steels and aluminum. The predicted locations of graphene/PVA composites with $0 \leq \phi_g \leq 3.5\%$ is also marked. This indicates the remarkable potential of graphene/PVA composites as ballistic materials: the best current materials have a $c^* \leq 500 \, \text{m s}^{-1}$, while Fig. 7b suggests that even an addition of 1 vol.% graphene into PVA is capable of surpassing this value. In fact a $\phi_g = 0.3$ graphene/PVA composite is predicted to have a c^* five times the best current composites. Graphene composites thus have an enormous potential as ballistic resistant materials though of course it remains to be seen whether such defect-free composites with large and aligned flake are manufacturable on a scales to make them practically viable.

7. Concluding remarks

A method to manufacture composites comprising a polyvinyl alcohol (PVA) matrix reinforced by ~35 vol.% multilayer graphene (MLG) was developed. The MLG comprised ~30 graphene layers and the resulting conductive composite has as reduced the strain-rate sensitivity and higher strengths at lower strain rates compared to the PVA matrix. However, the ductility of the composite however was lower than the PVA although the toughness of the composite was similar to that of aluminum. Nevertheless, the strength and stiffness of the composite are well below the predicted theoretical upper bounds. This is presumably due to defects such as poor platelet alignment and small graphene platelet sizes.

Edge clamped films of the composite have a ballistic limit that is V_{bl} that is nearly twice that of equal areal mass aluminum foils over the whole range of projectile masses investigated here. This ballistic limit is shown to be well captured by a membrane stretching analysis. This analysis is used to predict the ballistic performance of so-called ultimate graphene composites that comprise large aligned flakes and attain the theoretical maximum mechanical properties.

Such composites, if manufacturable, have the potential to have a ballistic limit in excess of three times the best high-performance commercial composites with only 10 vol.% graphene reinforcement in PVA.

Acknowledgements

References

[1] M. Xu, T. Liang, M. Shi, H. Chen, Graphene-Like Two-Dimensional Materials, Chem. Rev. 113 (2013) 3766–3798. doi:10.1021/cr300263a.

[2] K.S. Novoselov, V.I. Fal′ko, L. Colombo, P.R. Gellert, M.G. Schwab, K. Kim, A roadmap for graphene, Nature. 490 (2012) 192–200. doi:10.1038/nature11458.

[3] M. Yi, Z. Shen, A review on mechanical exfoliation for the scalable production of graphene, J. Mater. Chem. A. 3 (2015) 11700–11715. doi:10.1039/C5TA00252D.

[4] K.R. Paton, E. Varrla, C. Backes, R.J. Smith, U. Khan, A. O'Neill, C. Boland, M. Lotya, O.M. Istrate, P. King, T. Higgins, S. Barwich, P. May, P. Puczkarski, I. Ahmed, M. Moebius, H. Pettersson, E. Long, J. Coelho, S.E. O'Brien, E.K. McGuire, B.M. Sanchez, G.S. Duesberg, N. McEvoy, T.J. Pennycook, C. Downing, A. Crossley, V. Nicolosi, J.N. Coleman, Scalable production of large quantities of defect-free few-layer graphene by shear exfoliation in liquids, Nat Mater. 13 (2014) 624–630. doi:10.1038/nmat3944.

[5] H. Kim, A.A. Abdala, C.W. Macosko, Graphene/Polymer Nanocomposites, Macromolecules. 43 (2010) 6515–6530. doi:10.1021/ma100572e.

[6] J.R. Potts, D.R. Dreyer, C.W. Bielawski, R.S. Ruoff, Graphene-based polymer nanocomposites, Polymer. 52 (2011) 5–25. doi:10.1016/j.polymer.2010.11.042.

[7] C.N.R. Rao, A.K. Sood, K.S. Subrahmanyam, A. Govindaraj, Graphene: The New Two-Dimensional Nanomaterial, Angewandte Chemie International Edition. 48 (2009) 7752–7777. doi:10.1002/anie.200901678.

[8] V. Singh, D. Joung, L. Zhai, S. Das, S.I. Khondaker, S. Seal, Graphene based materials: Past, present and future, Progress in Materials Science. 56 (2011) 1178–1271. doi:10.1016/j.pmatsci.2011.03.003.

[9] J. Liang, Y. Huang, L. Zhang, Y. Wang, Y. Ma, T. Guo, Y. Chen, Molecular-Level Dispersion of Graphene into Poly(vinyl alcohol) and Effective Reinforcement of their Nanocomposites, Adv. Funct. Mater. 19 (2009) 2297–2302. doi:10.1002/adfm.200801776.

[10] X. Zhao, Q. Zhang, D. Chen, Enhanced Mechanical Properties of Graphene-Based Poly(vinyl alcohol) Composites, Macromolecules. 43 (2010) 2357–2363. doi:10.1021/ma902862u.

[11] X. Yang, L. Li, S. Shang, X. Tao, Synthesis and characterization of layer-aligned poly(vinyl alcohol)/graphene nanocomposites, Polymer. 51 (2010) 3431–3435. doi:10.1016/j.polymer.2010.05.034.

[12] J. Wang, X. Wang, C. Xu, M. Zhang, X. Shang, Preparation of graphene/poly(vinyl alcohol) nanocomposites with enhanced mechanical properties and water resistance, Polym. Int. 60 (2011) 816–822. doi:10.1002/pi.3025.

[13] I. Tantis, G.C. Psarras, D. Tasis, Functionalized graphene – poly(vinyl alcohol) nanocomposites: Physical and dielectric properties, eXPRESS Polymer Letters. 6 (2012) 283–292. doi:10.3144/expresspolymlett.2012.31.

[14] S. Morimune, T. Nishino, T. Goto, Poly(vinyl alcohol)/graphene oxide nanocomposites prepared by a simple eco-process, Polym J. 44 (2012) 1056–1063. doi:10.1038/pj.2012.58.

[15] J.-H. Lee, P.E. Loya, J. Lou, E.L. Thomas, Dynamic mechanical behavior of multilayer graphene via supersonic projectile penetration, Science. 346 (2014) 1092–1096. doi:10.1126/science.1258544.

[16] M.E. Backman, W. Goldsmith, The mechanics of penetration of projectiles into targets, International Journal of Engineering Science. 16 (1978) 1–99. doi:10.1016/0020-7225(78)90002-2.

[17] R. Vermorel, N. Vandenberghe, E. Villermaux, Impacts on thin elastic sheets, Proceedings of the Royal Society of London A: Mathematical, Physical and Engineering Sciences. 465 (2009) 823–842. doi:10.1098/rspa.2008.0297.

[18] B.A. Cheeseman, T.A. Bogetti, Ballistic impact into fabric and compliant composite laminates, Composite Structures. 61 (2003) 161–173. doi:10.1016/S0263-8223(03)00029-1.

[19] K. Karthikeyan, B.P. Russell, N.A. Fleck, M.R. O'Masta, H.N.G. Wadley, V.S. Deshpande, The soft impact response of composite laminate beams, International Journal of Impact Engineering. 60 (2013) 24–36. doi:10.1016/j.ijimpeng.2013.04.002.

[20] K. Karthikeyan, B.P. Russell, Polyethylene ballistic laminates: Failure mechanics and interface effect, Mater Des. 63 (2014) 115–125. doi:10.1016/j.matdes.2014.05.069.

[21]   S.L. Phoenix, P.K. Porwal, A new membrane model for the ballistic impact response and V50 performance of multi-ply fibrous systems, International Journal of Solids and Structures. 40 (2003) 6723–6765. doi:10.1016/S0020-7683(03)00329-9.

[22]   C. Lee, X. Wei, J.W. Kysar, J. Hone, Measurement of the Elastic Properties and Intrinsic Strength of Monolayer Graphene, Science. 321 (2008) 385–388. doi:10.1126/science.1157996.

[23]   CES EduPack, Granta Design Limited, 2015.

[24]   ASTM D1938, Standard Test Method for Tear-Propagation Resistance (Trouser Tear) of Plastic Film and Thin Sheeting by a Single-Tear Method, ASTM International, West Conshohocken, PA, 2014. www.astm.org.

[25]   P.M. Cunniff, Dimensionless parameters for optimization of textile-based body armor systems, in: W.G. Reinecke (Ed.), Proceedings of the 18th International Symposium on Ballistics, Technomic Publishing Company, Inc, San Antonio, TX, 1999: pp. 1303–1310.

[26]   M.R. O'Masta, D.H. Crayton, V.S. Deshpande, H.N.G. Wadley, Indentation of polyethylene laminates by a flat-bottomed cylindrical punch, Composites Part A: Applied Science and Manufacturing. 80 (2016) 138–147. doi:10.1016/j.compositesa.2015.10.015.

[27]   A.K. Bandaru, V.V. Chavan, S. Ahmad, R. Alagirusamy, N. Bhatnagar, Ballistic impact response of Kevlar® reinforced thermoplastic composite armors, International Journal of Impact Engineering. 89 (2016) 1–13. doi:10.1016/j.ijimpeng.2015.10.014.

[28]   Hexcel Corp., HexPly 8552: Product Data, (2016). http://www.hexcel.com/Resources/DataSheets/Prepreg-Data-Sheets/8552_eu.pdf.

[29]   Toray Carbon Fibers America, Inc., T800H Data Sheet, 2016. http://www.toraycfa.com/pdfs/T800HDataSheet.pdf.

[30]   M.R. O'Masta, D.H. Crayton, V.S. Deshpande, H.N.G. Wadley, Mechanisms of penetration in polyethylene reinforced cross-ply laminates, International Journal of Impact Engineering. 86 (2015) 249–264. doi:10.1016/j.ijimpeng.2015.08.012.

[31]   M.R. O'Masta, V.S. Deshpande, H.N.G. Wadley, Defect controlled transverse compressive strength of polyethylene fiber laminates, International Journal of Solids and Structures. 52 (2015) 130–149. doi:10.1016/j.ijsolstr.2014.09.023.

[32]   B.D. Cullity, S.R. Stock, Elements of X-Ray Diffraction, Third Edition, Prentice Hall, Upper Saddle River, NJ, 2001.

Supplementary information, S1: X-ray diffraction measurement

Acquisition of the diffraction pattern employed a Philips X'Pert PW3020 X-ray diffractometer running a Bragg-Brentano scan in reflection mode. The X-ray radiation source was monochromated Cu Kα (wavelength of $\lambda = 0.154$ nm), generated using an accelerating voltage of 40 kV and a tube current of 40 mA. Samples, measuring 30 mm x 30 mm, were mounted flat against a silicon wafer, and scanned over a diffraction angle of $2\theta = 14°$ to $34°$ in steps of $0.05°$.

Figure S1 shows a representative diffraction pattern of the MLG/PVA film. The broad diffraction peak at $2\theta \approx 19°$ was from PVA, as verified from a separate scan of the pure PVA film (Fig. S1). Using Bragg's law (i.e. $\lambda = 2d_{hkl} \sin \theta_{hkl}$), the peak at $2\theta = 26.4°$ is identified as the (002) peak of graphite, with an interatomic spacing of $d_{002} = 3.37$ Å. For small crystals, a lower bound estimate of the crystal size normal to the diffraction plane can be calculated from the full-width half-mass, B, of the diffraction curve, using Scherrer's formula: $l_{hkl} = K\lambda/(B \cos \theta_{hkl})$, where K is a shape factor with a typical value of 0.9 [32]. Instrumental line

broadening was <0.1°, as measured using a LaB6 standard, and, as such, considered negligible (within experimental error). From an average of five samples, the interatomic spacing was 0.84° ± 0.07°, revealing of an average of 29 ± 3 graphene layers per graphite platelet (given by l_{002}/d_{002}).
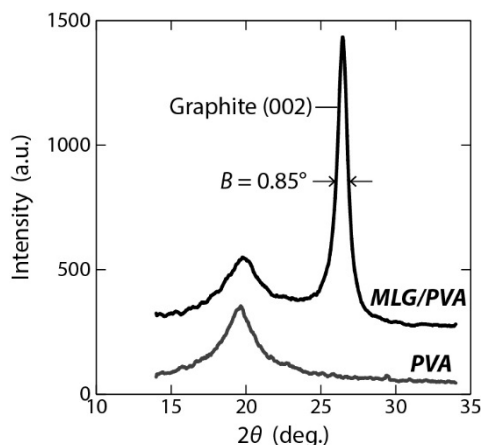

Figure S1: Representative X-ray diffraction patterns of MLG/PVA and PVA films. The graphite (002) full-width half mass, B, is identified.

Supplementary information, S2: Tear toughness measurement

Toughness measurement of each film was performed using the trouser tear test as given by ASTM standard D1938 [24]. The coupon measured 12 mm × 36 mm and had a 24 mm slit down the centerline of the long axis (Fig. S2). Each leg was gripped by a wedge action grip, and the coupon pulled apart in tension at a constant rate of displacement of $\dot{u} = 250$ mm min^{-1} by a model 5544 Instron equipped with a 5 N load cell. A representative response of each film is shown in Fig. S2. The steady-state load normalized by the film half-thickness gives the tear resistance.
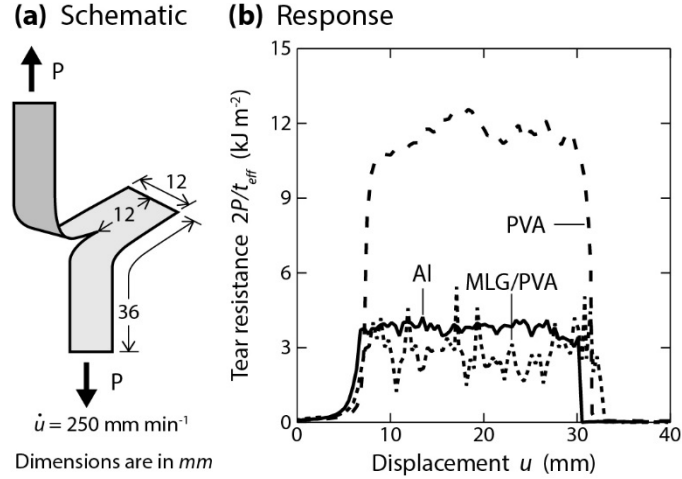
(a) Schematic   **(b)** Response

$\dot{u} = 250$ mm min^{-1}

Dimensions are in *mm*

Tear resistance $2P/t_{eff}$ (kJ m^{-2})

Displacement u (mm)

Figure S2: (a) Sketch of the trouser tear toughness experiment, and (b) representative load *P* versus displacement *u* responses of the three films investigated here.

Supplementary information, S3: Conductivity measurement

The electrical conductivity Σ_c of the MLG/PVA films was measured using four-terminal sensing (Fig. S3). The current *I* supplied at the outer two connections was varied from 5 to 50 µA and was measured to a 0.1 µA precision using an ammeter placed in series with the current source. The voltage *V* was sensed across the inner connections using a voltmeter with a sensitivity of 0.01 V. The voltage was observed to vary linearly with the imposed current and hence the Σ_c calculated using via

$$\Sigma_c = \frac{I}{V}\frac{L}{Wt_c}, \qquad\qquad \text{(S1)}$$

where $L = 20$ mm is the separation distance between the inner sensing probes, $W = 10$ mm is the width of the film and t_c is the effective thickness of the film given in Table 1.
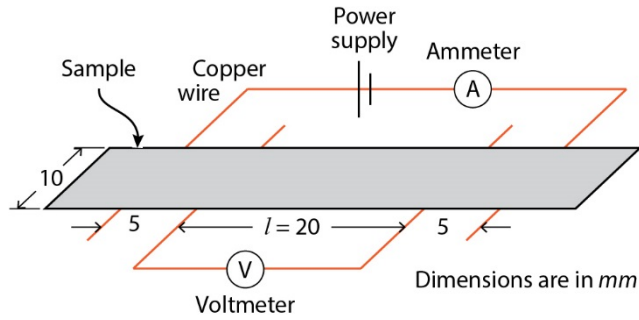
Figure S3: Sketch of the four-terminal sensing experiment used to measure the conductivity of the MLG/PVA composite films.

Supplementary information, S4: Projectile impact (PI) measurement

The projectile was launched by a custom designed two-compartment gas-gun as sketched in Fig. S4. Here we briefly describe the construction and operation of the gun. A type 6011 Burkert (Ingelfingen, Germany) solenoid valve released a reservoir of pressurized air that accelerated a sabot-encased rod (ram) down the first compartment of the barrel. At the end of the first compartment, the ram impacted the projectile resting in the narrower second compartment and accelerated the projectile down the remainder of the barrel. This two compartment set-up prevented air from loading the film prior to impact by the projectile. Both the reservoir pressure (variable between 8 and 21 bar) and the ram position along the 250 mm long first compartment of the barrel controlled the impact velocity V_0 of the projectile.
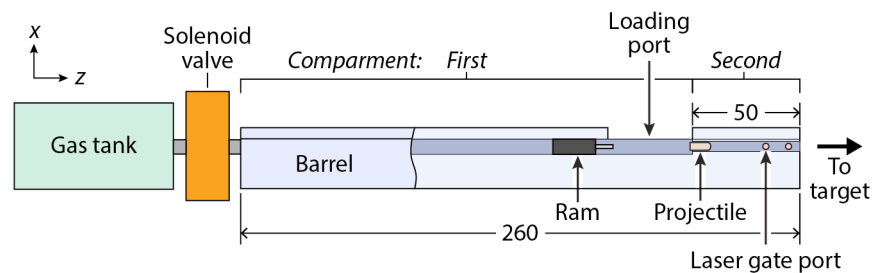

Figure S4: A side-view sketch of the gas-gun used for the projectile impact (PI) experiment. A cut away shows the interior of the double barrel. All dimensions are in mm.

The target was placed 30 mm down range from the muzzle end of the barrel as shown in Fig. 4c. This was sufficiently close to preclude yaw of the projectile or a reduction in projectile velocity from air drag. A model v1610 Phantom (Vision Research, Bedford, UK) high-speed camera aligned normal to the film captured the deformation of the rear surface. A pair of laser gates separated by 10 mm (Fig. S4) was used to estimate the velocity of the projectile as it exited the barrel. A few select tests with the high-speed camera set up for a side view were performed to confirm that these exit velocity measurements were equal to the velocity V_0 at which the projectile impacted the films.